JVI
Journals.ASM.org

Structural Insights into Adeno-Associated Virus Serotype 5

Lakshmanan Govindasamy,[a] Michael A. DiMattia,[a]* Brittney L. Gurda,[a]* Sujata Halder,[a] Robert McKenna,[a] John A. Chiorini,[b] Nicholas Muzyczka,[c] Sergei Zolotukhin,[d] Mavis Agbandje-McKenna[a]

Department of Biochemistry and Molecular Biology, Center for Structural Biology, McKnight Brain Institute, College of Medicine, University of Florida, Gainesville, Florida, USA[a]; MPTB, NIDCR, National Institutes of Health, Bethesda, Maryland, USA[b]; Department of Molecular Genetics and Microbiology and Powell Gene Therapy Center, College of Medicine, University of Florida, Gainesville, Florida, USA[c]; Department of Pediatrics, Division of Cell and Molecular Therapy, College of Medicine, University of Florida, Gainesville, Florida, USA[d]

The adeno-associated viruses (AAVs) display differential cell binding, transduction, and antigenic characteristics specified by their capsid viral protein (VP) composition. Toward structure-function annotation, the crystal structure of AAV5, one of the most sequence diverse AAV serotypes, was determined to 3.45-Å resolution. The AAV5 VP and capsid conserve topological features previously described for other AAVs but uniquely differ in the surface-exposed HI loop between βH and βI of the core β-barrel motif and have pronounced conformational differences in two of the AAV surface variable regions (VRs), VR-IV and VR-VII. The HI loop is structurally conserved in other AAVs despite amino acid differences but is smaller in AAV5 due to an amino acid deletion. This HI loop is adjacent to VR-VII, which is largest in AAV5. The VR-IV, which forms the larger outermost finger-like loop contributing to the protrusions surrounding the icosahedral 3-fold axes of the AAVs, is shorter in AAV5, creating a smoother capsid surface topology. The HI loop plays a role in AAV capsid assembly and genome packaging, and VR-IV and VR-VII are associated with transduction and antigenic differences, respectively, between the AAVs. A comparison of interior capsid surface charge and volume of AAV5 to AAV2 and AAV4 showed a higher propensity of acidic residues but similar volumes, consistent with comparable DNA packaging capacities. This structure provided a three-dimensional (3D) template for functional annotation of the AAV5 capsid with respect to regions that confer assembly efficiency, dictate cellular transduction phenotypes, and control antigenicity.

Recombinant adeno-associated viruses (rAAVs) are promising viral vectors for gene delivery applications (1, 2). These viruses belong to the single-stranded DNA (ssDNA)-packaging *Parvoviridae* and genus *Dependovirus*. Hundreds of AAV genotypes have been sequenced from several mammalian species, and to date 12 serotypes (AAV1 to AAV12) have been defined for the human and nonhuman primate isolates (3–15). The 12 serotypes are classified into eight genetic groups, clades A to F and clonal isolates AAV4 and AAV5, based on antigenic reactivity and sequence similarity (15). The groups are represented by AAV1 to AAV9, with AAV1 and AAV6 belonging to the same clade A because of their high sequence similarity and antigenic cross-reactivity. The representative members share ~55 to 99% sequence identity, with AAV4 and AAV5 being the most divergent from each other and from the other members.

The linear ssDNA AAV genome, ~4.7 kb in length, contains two genes: *cap*, which encodes the capsid viral proteins (VPs; VP1, ~87 kDa; VP2, ~73 kDa; VP3, ~62 kDa) and *rep*, which encodes the replication proteins necessary for genome replication and genome packaging. Inverted terminal repeats (ITRs) at the end of the AAV genome, 145 bp in length, are the only essential active sequence required to function as (i) the origin for DNA replication, (ii) the packaging signal, and (iii) integration sites (16–19). Recombinant AAV gene delivery vectors contain a genome in which the ITRs are retained, but the wild-type AAV coding sequence is replaced with a therapeutic gene (the transgene). These vectors are assembled by the addition of plasmid constructs encoding the VP and Rep proteins in *trans*. The AAV capsids have a T=1 icosahedral symmetry and contain 60 subunits, in total, of VP1, VP2, and VP3 (in a predicted ratio of 1:1:10) translated from the same mRNA. Therefore, the VPs are overlapping, with VP1 and VP2 sharing their C-terminal sequences with VP3 (~520 amino acids [aa]) but containing additional N-terminal sequences not present in VP3. VP1 has a unique N-terminal region (VP1u) of ~137 aa.

Structures determined for AAVs show capsids assembled from the common VP3 region (20–29). There is currently no experimentally determined structure for VP1u or the overlapping VP1/VP2 N terminus. Low-resolution density globules located inside the capsid under the icosahedral 2-fold axes have been interpreted as the VP1u (25, 28). The VP3 topology contains a core eight-stranded (βB to βI) β-barrel motif and large loop insertions between the β-strands which form the surface of the capsid. Conformational variations in these surface loops (VR-I to VR-IX [22]) define the unique surface features for the each of the six representative AAV capsid structures, AAV2, AAV3B, AAV4, AAV6, AAV8, and AAV9, previously determined by X-ray crystallography (21–23, 26, 27, 29).

Several wild-type AAV isolates as well as chimeras generated by directed evolution or rational mutagenesis are actively being developed for gene delivery applications (e.g., reviewed in reference 2). Transgenes packaged within the prototype human serotype

Received 30 March 2013 **Accepted** 1 August 2013
Published ahead of print 7 August 2013

Address correspondence to Mavis Agbandje-McKenna, mckenna@ufl.edu.

* Present address: Michael A. DiMattia, NIH, NIAMS, Laboratory of Structural Biology Research, Bethesda, Maryland, USA; Brittney L. Gurda, Gene Therapy Program, Department of Pathology and Laboratory Medicine, Division of Transfusion Medicine, University of Pennsylvania, Philadelphia, Pennsylvania, USA.

doi:10.1128/JVI.00867-13

AAV2 have been effective for the correction of genetic diseases of the eye, brain, muscle, liver, and lung in animal models and successfully used for the treatment of human blindness and muscular dystrophy (see references 30 to 42). However, other serotypes show capsid sequence-associated improved gene delivery for certain tissues compared to AAV2. As an example, in studies in which the same transgene is packaged, AAV5 is more efficient than AAV2 at transducing neuronal and lung tissues (43–45). In the apical surface of the airway epithelia, AAV5 shows 20 and 50 times better transduction than AAV2, *in vivo* and *in vitro*, respectively, and is equally as effective as AAV8 in systemic expression of coagulation factor IX for the treatment of hemophilia (44, 46). These observations have fueled efforts to develop AAV5 as a vector for treatment of genetic disease (see references 47 to 50). This, in turn, has resulted in efforts to characterize AAV5 in terms of its capsid structure and its cellular interactions that dictate its improved transduction phenotype.

The best-characterized serotype with respect to functional regions of the AAV VP or capsid is AAV2, facilitated by the available crystal structure of this serotype (21). The structural differences that have been described between the AAVs are mostly associated with regions in AAV2 that dictate receptor attachment and tissue tropism, transduction efficiency, and antigenic diversity between the serotypes (reviewed in references 22, 26, 27, 29, 51, and 52). Thus, efforts to improve the therapeutic efficacy of gene delivery applications can benefit from capsid manipulation aided by structural information and identification of the capsid regions that confer unique serotype properties. In this study, the high-resolution crystal structure of AAV5, one of the most divergent serotypes in terms of sequence and antigenicity (as is AAV4) and a promising vector for gene therapy, was determined by X-ray crystallography to provide a three-dimensional (3D) platform for further annotation of AAV functional domains. In addition to the nine variable regions (VRs) VR-I to VR-IX previously described when the crystal structures of AAV2 and AAV4 were compared, additional surface loop regions have been identified that uniquely differ in AAV5 compared to other AAVs. These capsid conformational differences likely confer serotype-specific functionality involving receptor attachment, tissue transduction, and capsid assembly phenotype. In contrast to the variability observed on the exterior surface of the AAV5 capsid, the internal surface topology and the volume it encloses are highly conserved compared to those of AAV2 and AAV4. The comparable volume is inconsistent with a report that AAV5 is capable of packaging a genome that is ~50% larger than the capacity for other AAVs (53) and is consistent with later observations of a maximal packaging capacity that is comparable to that of other AAVs (54–56). The AAV5 structure also provided a 3D template for the comparison of the AAV5-like virus, AAV-Go.1 (13), enabling the identification of potential antigenic regions on the virus capsid clustered around the protrusions surrounding the icosahedral 3-fold axes.

MATERIALS AND METHODS

Data collection and processing. The production, purification, and preliminary X-ray crystallographic studies of the AAV5 capsids have been previously described (57). Briefly, a total of 500 0.3°-oscillation diffraction images were collected from 10 frozen crystals, grown from baculovirus-expressed virus-like particles (VLPs) assembled from VP1, VP2, and VP3, at three different synchrotron beam lines: F1 at the Cornell High Energy Synchrotron Source (CHESS, Cornell University, Ithaca, NY), X29 at the National Synchrotron Light Source (NSLS) at the Brookhaven National Laboratory, and 22-ID at the Advanced Photon Source (APS) at the Argonne National Laboratory. The diffraction data were processed, scaled, and reduced with the HKL package (58). The crystals belong to the orthorhombic space group $P2_12_12_1$ with unit cell dimensions of $a = 264.7$, $b = 447.9$, and $c = 629.7$ Å. The final data set consisted of a total of 762,314 independent reflections for data between 50.0- and 3.45-Å resolution, with an R_{sym} of 16.4% and an overall completeness of 78.6% (57).

Structure determination and refinement. The structure was initially phased by molecular replacement procedures utilizing cross-rotation and translation function search procedures with the crystal structure of AAV4 (Protein Data Bank [PDB] accession number 2G8G) as a phasing model as previously reported (57). There are four complete VLPs in the unit cell and one particle (assembled from 60 VP monomers) per crystallographic asymmetric unit. An AAV4 polyalanine icosahedral particle model, containing 60 VP3 monomers, was oriented and positioned in the crystal unit cell based on the molecular replacement solution. Initial phases were calculated, and the initial model was improved using the simulated annealing, energy minimization, and conventional positional refinement subroutines, followed by real-space electron density map averaging, using a molecular mask, while applying strict 60-fold noncrystallographic symmetry (NCS), in the CNS program (59). A subset of reflections (5%) was partitioned for monitoring of the refinement process (60). An AAV5 VP3 polypeptide model was built into averaged Fourier $2F_o - F_c$ and $F_o - F_c$ (where F_o is the observed structure factor and F_c is the structure factor calculated from the model) electron density maps using the molecular graphics programs O (61) and Coot (62), based on the published amino acid sequence (4). A total of 516 amino acid residues, interpreted as positions 209 to 724 (VP1 numbering) of the AAV5 VP, were fitted into the NCS-averaged $2F_o - F_c$ electron density maps by substitution, insertion, and deletion of amino acids with respect to the AAV4 polyalanine phasing model. There was no ordered electron density observed for residues 1 to 208. New phases were then calculated using this improved model and further improved by alternating cycles of refinement and model building into averaged electron $2F_o - F_c$ density maps (59, 61, 62), with the map subjected to density modification after each round of refinement in the CNS program. The refinement was deemed to have converged when there was no further improvement in the overall agreement between the observed and calculated structure factors (R_{work}, defined in Table 1), and the averaging correlation coefficient was ~0.9. Additional omit ($F_o - F_c$) density inside a pocket formed between two VP monomers was interpreted as a glycerol molecule. Further uninterpreted high sigma density ($\sigma > 3.5$) regions were modeled and refined as sodium ions or solvent molecules. The CNS-refined AAV5 VP model (residues 209 to 724 in the VP3 common sequence) was used to calculate average temperature factors (B factors) and the root mean square deviation (RMSD) from ideal bond lengths and angles using the CNS program (59) and from main-chain torsion angles using the PROCHECK program (63). Temperature factors were also calculated for the glycerol, sodium atoms, and solvent molecules to confirm their assignment.

Following the AAV5 VP structure refinement/rebuilding procedures in the CNS program (i.e., at the stage where this procedure was deemed complete [see above]), the refinement protocol was continued in the PHENIX program following reports of improved refinement statistics using this application (64). Ten individual macrocycles, following the protocol of individual coordinates and atomic displacement parameter refinement, were carried out using strict NCS restraints, and the target weights were optimized by PHENIX (64). Bulk-solvent correction was applied throughout the refinement process, and the Resolve program was used for electron density modification and molecular averaging, followed by map visualization and model improvement in Coot (62). The PHENIX program outputs the RMSD from ideal bond lengths and angles for the refined model. The use of the PHENIX program for the final rounds of structural refinement improved the R_{work} value by ~3% (from 28.3% to 25.2%), with a modest improvement in the molecular geometry of the

TABLE 1 Summary of structure refinement statistics

Parameter	Value for the parameter
R_{work}/R_{free} [a]	0.25/0.25
RMSDs	
Bond length (Å)	0.005
Angle (°)	1.15
Wilson B factor (Å^2)	47
Total no. of atoms	
Protein	4,111
Glycerol	6
Sodium	3
Avg B factors (Å^2)	
Protein	55.3
Glycerol	50.1
Sodium	12.4
Solvent	25.9
Ramachandran plot statistics (%)	
Most favored	89.9
Additional allowed	9
Generously allowed	0.7
Outliers	0.2
MolProbity validation of Ramachandran plot (%)	
Allowed regions	99.8
Disallowed regions	0.2
PDB accession no.	3NTT

[a] $R_{cryst} = \sum ||F_o| - |F_c||/\sum |F_o|$, where $|F_o|$ and $|F_c|$ are the observed and calculated structure factor amplitudes, respectively; R_{free} is calculated using the 5 % of reflections excluded from the overall data set during refinement.

VP3 structure (from RMSDs in bond length and bond angle changes of 0.008 to 0.005 Å and 1.48 to 1.15°, respectively) compared to the CNS program. The average temperature factors for the main and side chains were computed using the UPPSALA Software Factory MOLEMAN program (65). The AAV5 model was validated with the Coot, MolProbity, and PROCHECK programs (62, 63, 66). The refinement statistics are given in Table 1.

AAV structural comparisons. The AAV5 VP3 structure was compared to the structures of AAV2 (PDB accession number 1LP3) and AAV4 (PDB accession number 2G8G) by structural alignment with the secondary-structure matching (SSM) program (67).The program superposes Cα positions and provides information on residues that are structurally equivalent, inserts gaps when the atoms are too far apart to superpose, and provides the distances (in Å) between the Cα positions. Conformationally distinct regions were identified as previously defined (22) as being regions of more than two amino acids with Cα positions that are greater than 1.0 Å apart between two different serotypes. An additional visual comparison of the superposition of the structures was carried out using the Coot program (62). The available crystal structures of AAV3b, AAV6, AAV8, and AAV9 (23, 26, 27, 29) were not included in this analysis due to their high similarity to AAV2 and the fact that regions which vary between them and AAV2 were already described when this serotype was compared to AAV4.

Calculation of internal capsid volume. The internal volume of the AAV2, AAV4, AAV5, and human parvovirus B19 (PDB accession number 1S58) capsids were calculated from the radius of the capsid interior. This value was estimated from the average of the distances between the capsid center and the innermost position of the capsid protein shell at the icosahedral 2-, 3-, and 5-fold axes. Exterior and interior capsid surface charges were estimated based on the number of acidic (aspartic acid and glutamic acid) and basic (arginine, lysines, and histidine) residues and the assignment of minus 1 (aspartic acid and glutamic acid), plus 1 (arginine and lysine), or plus 0.5 (histidine) charges based on a surface "Roadmap" (68).

Three-dimensional model building for homologous AAV-Go.1. A homology model was generated for VP3 amino acid sequences of vertebrate AAV-Go.1 (13) using the AAV5 structure. The model was generated using the SWISS-MODEL program (69) with the AAV5 structure supplied as a template. The AAV-Go.1 model was compared to AAV2 and AAV5 to identify VP/capsid regions that are common to or variable in these viruses. The Coot program (62) was used for visual structural comparisons, and the Roadmap program (68) was used for displaying the surface positions of amino acid differences between AAV5 and AAV-Go.1. A sequence alignment of AAV-Go.1 with AAV2 and AAV5 was also conducted using the CLUSTAL W application in the EXPASY Proteomics Server (http://expasy.org/tools/) (70).

Protein structure accession number. The refined AAV5 coordinates have been deposited in the Protein Data Bank under accession number 3NTT.

RESULTS AND DISCUSSION

The AAV5 crystal structure. The crystal structure of AAV5 VLPs was determined to 3.45-Å resolution. Residues 209 to 724 of the VP3 common region (here after referred to as VP3) were assigned into the NCS-averaged electron density maps (example section shown in Fig. 1A). This structure enabled the high-resolution interpretation of amino acid side chains, surface loop regions, and secondary structure elements (Fig. 1B) in contrast to the lower-resolution cryo-electron microscopy and image-reconstructed (cryo-reconstructed) structure and pseudoatomic model previously published for AAV5 (24). Residue 724 is the last C-terminal amino acid. The first 208 amino acids of the VP, comprising the VP1 unique region with a phospholipase A2 domain, the VP1/VP2 common region (residues 137 to 192), and the first 15 residues of VP3, are not observed. This lack of N-terminal VP ordering is consistent with all reported parvovirus structures determined to date, other than the cryo-reconstructed structure of human parvovirus B19 in which the N-terminal residues of VP2 were observed (71). Two possible explanations for the lack of ordering of the N-terminal residues in parvovirus crystal structures are that the copy numbers of VP1 and VP2 in the capsid are low relative to VP3 and/or that the N termini of VP1, VP2, and VP3 adopt distinct conformations. These possibilities are incompatible with the NCS averaging utilized during structure determination. Sixty copies of the ordered VP region, residues 209 to 724, assemble the AAV5 capsid (Fig. 2A).

Unlike the structures determined for some other AAV capsids, for example, AAV3B, AAV4, AAV6, and AAV8, including VLPs produced in baculovirus/Sf9 expression systems (e.g., AAV6 and AAV8), where at least one DNA nucleotide is ordered (22, 23, 26, 27, 29), there was no DNA ordered in the AAV5 capsid interior in the previously identified DNA binding pocket, despite the conservation of the binding pocket amino acids. The lack of ordering of a nucleotide in AAV5 is predicted to be due to the high radiation sensitivity of the thin crystals used for X-ray diffraction data collection.

The refinement statistics for the VP3 model, R_{work} and R_{free}, were both 0.25, as given in Table 1. The similarity of the R_{work} and R_{free} values is due to the high NCS of the capsid. These R values are comparable to or better than those quoted for other available par-

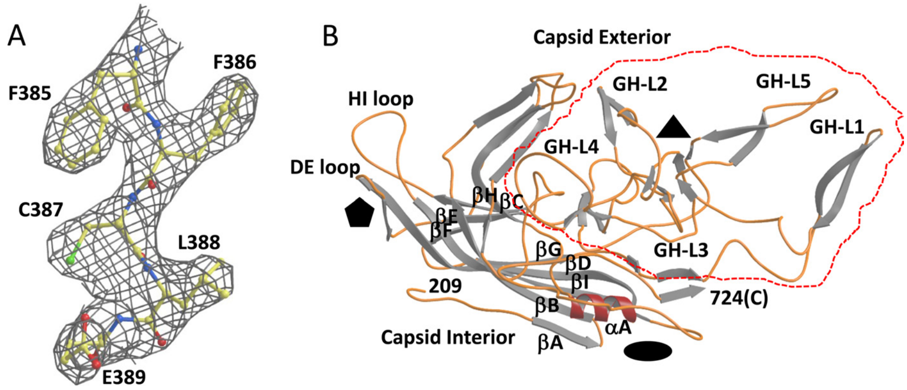

FIG 1 Structure of AAV5. (A) A section of the averaged $2F_o - F_c$ electron density map (gray mesh, contoured at a threshold of 1.0 σ) for residues 385 to 389 shown in stick form and colored according to atom type: C in yellow, N in blue, O in red, and S in green. (B) A ribbon diagram representation of the ordered overlapping VP3 monomer region (residues 209 to 724) of AAV5. The conserved β-barrel core motif (βBIDG-βCHEF, gray), conserved αA helix, DE loop (between βD and βE), HI loop (between βH and βI), and subloops between βG and βH (GH-L1 to GH-L5) are labeled. The approximate positions of the 2-, 3-, and 5-fold axes are indicated by the filled oval, triangle, and pentagon, respectively. The interior and exterior capsid surfaces are also indicated. The dashed red circle delineates the subloops within the GH loop. These images were generated using the PyMol program (http://www.pymol.org).

vovirus structures determined at comparable resolution, as reported on the VIPERdb website (http://viperdb.scripps.edu/). The stereochemical parameters and geometries of the AAV5 VP3 model (Table 1) are also consistent with those reported for other virus structures at comparable resolution.

AAV5 is assembled from conserved parvovirus VP features. The most highly conserved regions of the AAV5 VP3, with respect to the VPs of other parvovirus (including AAV) structures, is the eight-stranded (βBIDG-βCHEF sheets) antiparallel β-barrel structure and a helix, αA (Fig. 1B). The β-barrel forms the core of the capsid, with the βBIDG sheet forming the interior surface providing the enclosure for the packaged ssDNA (Fig. 2B, blue interior surface). Small stretches of antiparallel β-strands are also observed in the loops between the β-strands (Fig. 1B), as previ-

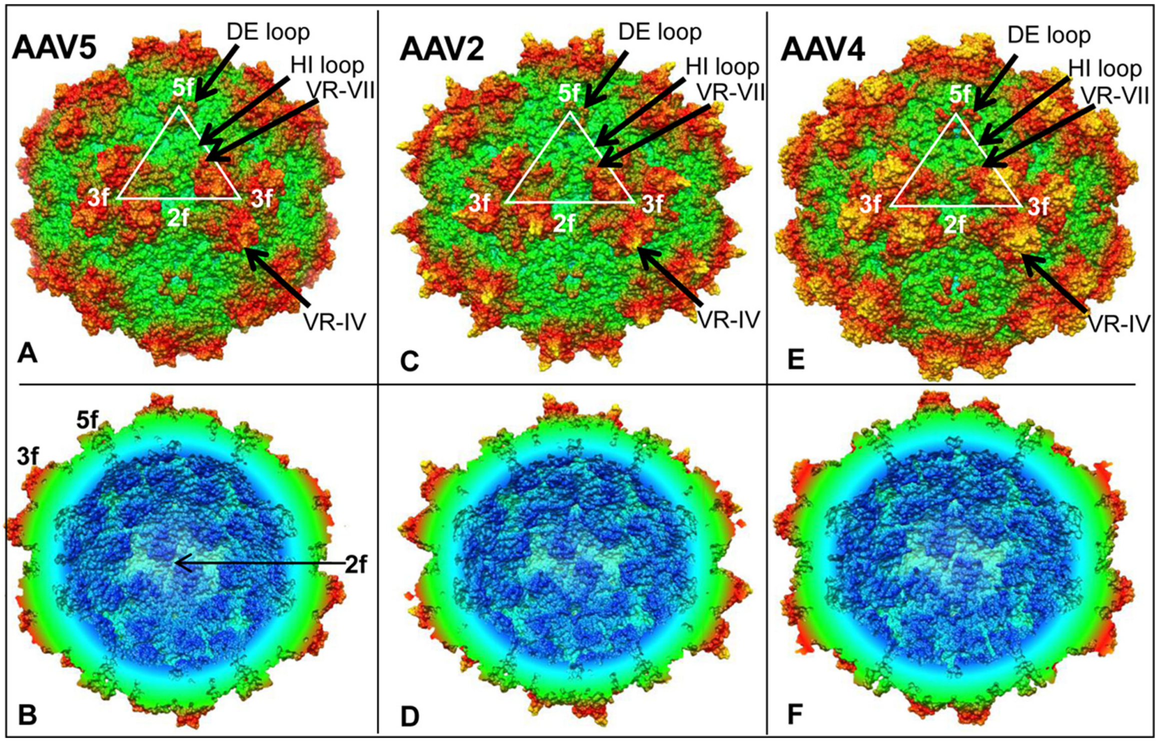

FIG 2 AAV capsid surfaces. (A, C, and E) Exterior capsid surfaces for AAV5, AAV2, and AAV4, respectively. The surfaces are radially color cued (from capsid center to surface: blue to green to red to yellow; ~80 to 140 Å). The white triangles depict the viral asymmetric units bounded by a 5-fold (5f) axis and two 3-fold (3f) axes divided by a line through a 2-fold (2f) axis. Example surface features that differ between AAV5 and the AAV2 and AAV4 compared are indicated: VR-IV, VR-VII, DE loop, and HI loop. (B, D, and F) Cross-sections of the AAV5, AAV2, and AAV4 capsids, respectively, showing their interior surfaces. The radial depth cue is as described for panels A, C, and E. The dark blue regions show the βA strand and βBIDG-sheet secondary-structure elements conserved in the three viruses. The 2-fold (2f) axis is indicated in AAV5. These images were generated using the CHIMERA program (118).

ously described in the structures of other AAVs (21–23, 26, 27, 29) and members of the autonomous parvoviruses (reviewed in references 72 and 73). The AAV5 αA helix (residues 283 to 294) is located close to the icosahedral 2-fold axis and forms the wall of the surface depression located at this capsid region (see below) (Fig. 1B).

The loops between the βB and βI strands extend away from the β-barrel core (Fig. 1B) and are responsible for forming the surface topology of the capsid (Fig. 2A). The clustering of these loop regions from icosahedral symmetry-related VP3 monomers forms the characteristic parvovirus capsid surface features. These include a depression at the icosahedral 2-fold axis, three protrusions surrounding the icosahedral 3-fold axis (which is located at a depression), and a depression surrounding the icosahedral 5-fold axis at which is centered a protruding cylindrical channel (Fig. 2A and B for AAV5, C and D for AAV2, and E and F for AAV4). The diameter of the capsid is 216 Å at the 2-fold axis, 223 Å at the 3-fold axis, 272 Å at the peak of the protrusions surrounding this axis, and 190 and 247 Å at the base and tip, respectively, of the cylindrical channel at the 5-fold axis. The 2-fold axis is formed by only one loop segment (residues 684 to 694) that intertwines with a symmetry-related loop (as described in reference 22). The floor of this depression is formed by the conserved αA (Fig. 1B), and the walls are formed by amino acid stretches 514 to 521, 548 to 553, and 711 to 721. The 3-fold axis is formed from amino acids on the descending side of subloop GH-L5 (residues 586 to 592) within the GH loop (containing ~230/724 VP amino acids) between strands βG and βH from icosahedral symmetry-related VP3 monomers (Fig. 1B). The three separate protrusions surrounding this axis (Fig. 2A) contain intertwining loops located within the GH loop: residues 435 to 452 (within GH-L1) and 566 to 586 (within GH-L5) from one VP3 monomer and residues 470 to 495 (within GH-L2) and 531 to 546 (within GH-L4) from the other monomer (Fig. 1B). The 5-fold axis is formed by a VP3 loop region consisting of two small stretches of β-structure (a β-ribbon) between the βD and βE strands (DE loop, residues 311 to 327) (Fig. 1B). The β-ribbon from each VP3 interacts with β-ribbons of four other VP3s to form the lining of the cylindrical channel that is conserved at the 5-fold axis in all AAV structures determined to date (Fig. 2A and B for AAV5, C and D for AAV2, and E and F for AAV4). This channel is also conserved in all other known parvovirus structures (72, 73). The HI loop, between βH and βI (residues 644 to 658), also conserved in all parvovirus structures, is located adjacent to the DE loop (Fig. 1B). This loop overlaps the surface of the CHEF sheet on the adjacent 5-fold-symmetry-related VP3 monomers to form the floor/surface of the depression surrounding the 5-fold channel (Fig. 1B and 2A, C, and E).

Structural comparison of AAV5 to AAV2 and AAV4 identifies variable regions that are unique to AAV5. Superposition of the AAV5 VP3 onto the VP3s of AAV2 and AAV4 clearly demonstrated that the nine VRs previously identified in comparing AAV4 to AAV2 (designated VR-I to VR-IX by Govindasamy et al. [22]) also differ between AAV5 and these two viruses (Fig. 3A). A number of these differences are due to deletions or insertions in the AAV5 amino acid sequence relative to the other two viruses (Fig. 3B). In two of the VRs, VR-IV (GH-L1) and VR-VII (GH-L4) (Fig. 1B), the AAV5 conformational variations are more pronounced than the differences between the other two AAVs (Fig. 3A and C). Variable region IV, which forms the outermost of the two finger-like VP loops contributing to the protrusions surrounding the icosahedral 3-fold axes, is shorter in AAV5 than in the other AAVs (Fig. 3A, C, E, and F) due to a deletion of six amino acids (Fig. 3B). Variable region VII, located at the base of each 3-fold protrusion close to the depression surrounding the 5-fold axis (Fig. 2A, C, and E), is larger in the VP3 of AAV5 than in the VP3s of AAV2 and AAV4, extending up to ~8 Å from the VR-VII loop residues in the other serotypes (Fig. 3A, C, E, and F). The AAV5 VR-VII loop contains three and two additional amino acids, respectively, compared to AAV2 and AAV4 (Fig. 3B). The HI loop structure, not previously defined as a VR, is unique in AAV5, differing from AAV2 and AAV4 (Fig. 3D) as well as AAV3B, AAV6, AAV8, and AAV9 (data not shown). The HI loop is structurally conserved in the other AAVs despite amino acid differences but is smaller in AAV5 due a residue deletion (Fig. 3A, B, and D). This HI loop is located adjacent to VR-VII from a 5-fold-symmetry-related monomer in the assembled capsid (Fig. 2A, C, and E and 4A). Significantly, the shorter VR-IV and the HI loop, VR-I, and VR-II differences compared to AAV2 were predicted from a pseudoatomic model of the AAV5 VP3 built into a 16-Å resolution cryo-reconstructed density map (24). However, the differences in VR-V to VR-IX (Fig. 3C) have only become evident in the crystal structure.

As reported for other AAV structures, the VRs are concentrated on the surface of the VP3 monomer and cluster to create local perturbations on the AAV5 capsid compared to the other AAV structures (Fig. 2A, C, and E) despite being distributed throughout the VP3 primary sequence and monomer structure (Fig. 3A and B and 4A). Variable regions VR-VI and VR-IX contribute to the wall of the depression at the icosahedral 2-fold axis (Fig. 3E and F), giving rise to capsid surface differences to the other AAV serotypes (Fig. 2A, C, and E). This depression is wider in AAV2, narrowest and deepest in AAV4, and almost nonexistent in AAV5 (Fig. 2A, C, and D). Variable regions I, III, VII, and IX (Fig. 3E and F) contribute to surface differences between the serotypes in the raised capsid surface region between the depression at the icosahedral 2-fold axis and surrounding the 5-fold axis (Fig. 2A, C, and E). Variable regions IV (within GH-L1) and VIII (within GH-L5) from one VP3 monomer and VR-V (within GH-L2) from a 3-fold-symmetry-related VP3 form the top of the three loops that comprise the protrusions which surround the 3-fold axes (Fig. 2A, C, and E). Variable region IV is larger and projects radially upward in AAV2, leading to more pointed finger-like 3-fold protrusions than found in AAV5 (compare in Fig. 2A and C, and 3A). The larger size of the AAV4 VR-IV and its "bent" conformation toward VR-VIII (Fig. 3A) result in larger and thicker protrusions around the 3-fold axes than in AAV5 (compare Fig. 2A and E and 3A). Variable region V is located between VR-IV and VR-VIII in the protrusion. Portions of VR-V in addition to VR-VI and VR-VII contribute to the formation of the base of the protrusions. In both AAV2 and AAV5, VR-V is smaller and structurally distinct from AAV4, which has additional amino acids (Fig. 3A, B, and C). Thus, the bases of the protrusions are narrower in AAV2 and AAV5 than in AAV4 (Fig. 2A and B for AAV5, C and D for AAV2, and E and F for AAV4). Variable region II is located at the top of a β-ribbon (DE loop) which forms the wall of the 5-fold channel (Fig. 1B, 2A, C, and E, and 3A). The β-ribbon is conserved in all AAV structures, but the VR-II difference in AAV5 results in an ~2.5-Å-diameter increase at the opening of its 5-fold channel compared to AAV2 and AAV4.

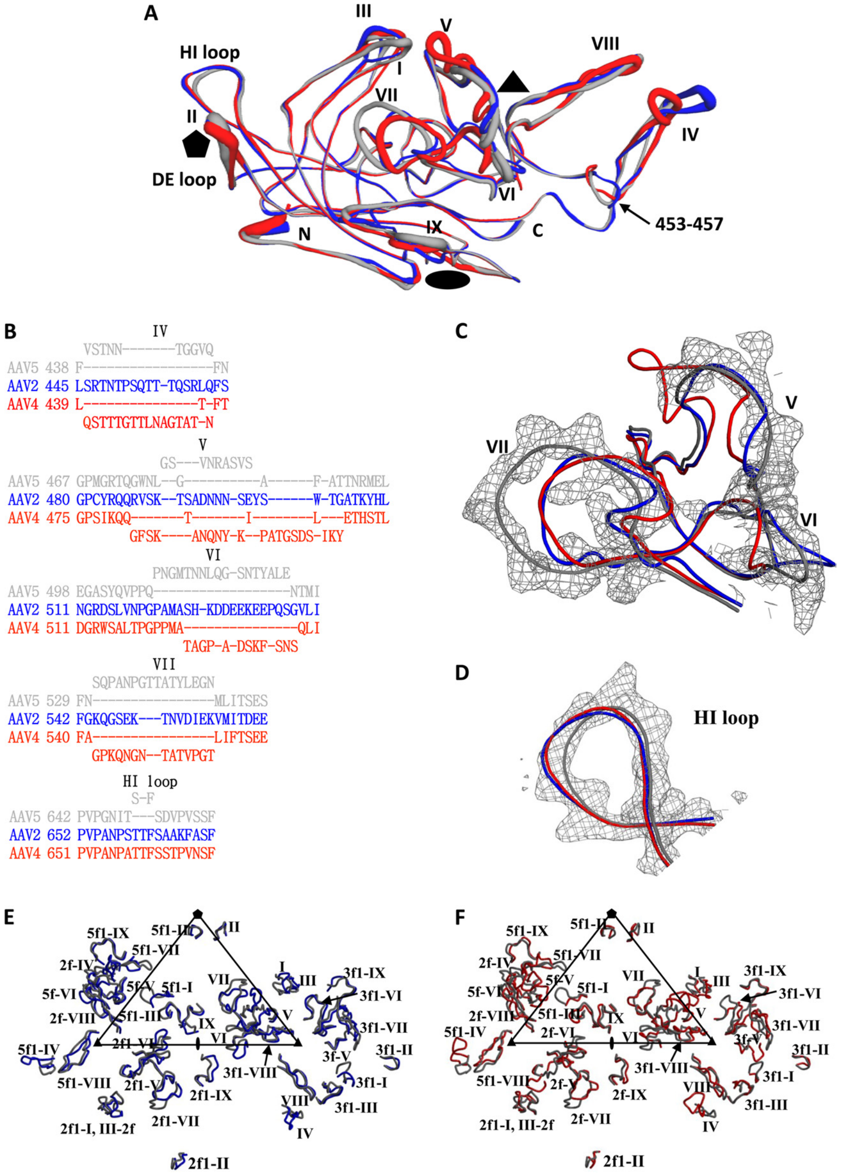

FIG 3 Unique features of the AAV5 VP3. (A) Superposition of the AAV2 (blue), AAV4 (red), and AAV5 (gray) VP3 monomer structures shown in a coil representation. A B factor (temperature factor) putty (thicker-coil) representation is used to show the regions of highest variability. The DE loop, HI loop, VR-I to VR-IX, and N and C termini are labeled. The approximate icosahedral symmetry axes are indicated as described in the legend of Fig. 1. (B) Structure-based sequence alignment of AAV2 (blue), AAV4 (red), and AAV5 (gray) for the amino acids in VR-IV, VR-V, VR-VI, VR-VII, and the HI loop. Regions of structural differences to AAV2 are offset above (for AAV5) or below (for AAV4) the alignment. (C) Superposition of the AAV2 (blue), AAV4 (red), and AAV5 (gray) VP3 structures at VR-V, VR-VI, and VR-VII (coil representation) within the averaged $2F_o - F_c$ electron density map of AAV5 (gray mesh) contoured at a threshold of 1.0 σ. (D) Superposition of the HI loop (coil representation) of the VP3 structures of AAV2 (blue), AAV4 (red), and AAV5 (gray) within the averaged $2F_o - F_c$ electron density map of AAV5 (gray mesh) contoured at a threshold of 1.0 σ. In panels C and D, amino acid side chains have been omitted for clarity. (E and F) Positions of VR-I to VR-IX within a viral asymmetric unit (defined in the legend of Fig. 2). The viral asymmetric unit contains contributions from the reference VP3 monomer and a 2-fold (2f), 3-fold (3f1), and 5-fold (5f1) (see reference 22 for definition of symmetry relationships) VP3 monomer (Fig. 1B). The prefixes on the labels for the variable regions indicate the contributing monomers. Panels A, C, and D were generated using the PyMol program (http://www.pymol.org), and panels E and F were generated using the Bobscript program (119) and rendered with the RASTER3D program (120, 121).

Unique features of AAV5 are stabilized by interactions with cations and glycerol. In addition to the VP3 density, a glycerol molecule and three Na^+ ions (Fig. 4A and B) and 46 solvent molecules per VP3 were ordered in the NCS-averaged AAV5 electron density map. The glycerol molecule, likely ordered from the 30% used as cryo-protectant during data collection (57), is located in a cleft at the base of the AAV5 VP3 VR-VII (discussed above), which is close to the HI loop from a 5-fold-symmetry-related VP monomer (Fig. 4A and B). The glycerol refined with atomic B factors that were similar to those of the VP atoms (Table 1). The molecule forms hydrogen bonds/polar interactions with the VP atoms as well as hydrophobic interactions. The three hydroxyl groups participate in interactions with the side chain of R277 (2.6 Å), the main-chain carbonyl oxygen of N530 (3.3 Å), the main-chain car-

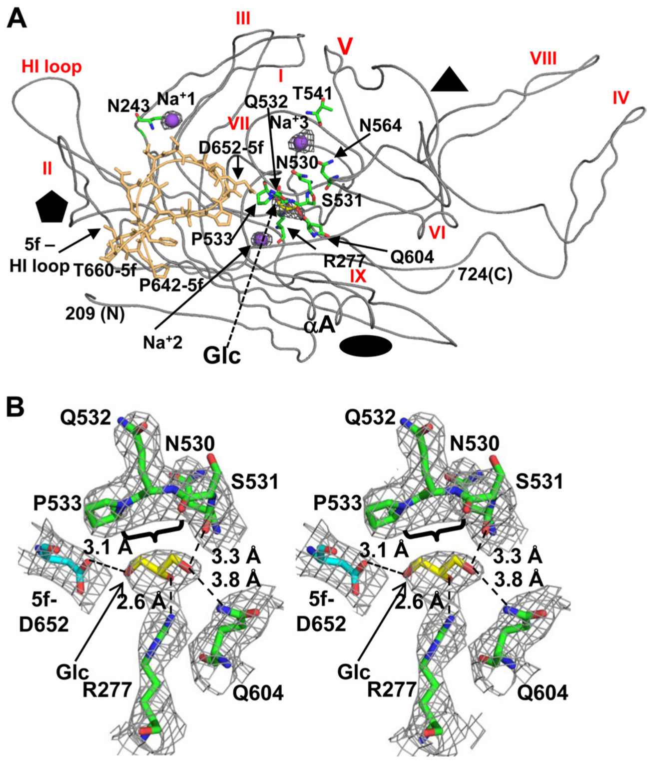

FIG 4 AAV5 capsid interactions with glycerol and cations. (A) A coil representation of the AAV5 VP3 (gray) with the HI loop (stick representation) from a 5-fold-symmetry-related VP3 monomer (wheat). The ordered glycerol molecule and three Na^+ ions are shown in the averaged AAV5 $2F_o - F_c$ electron density map (gray mesh) contoured at a threshold of 1.0 σ. The side chains for the amino acids interacting with the glycerol and Na^+ ions are shown in stick representation colored according to atom type (C in green, N in blue, and O in red) and labeled. The HI loop and VR-I to VR-IX are labeled. The approximate icosahedral symmetry axes are indicated as described in the legend of Fig. 1. (B). Stereo view of the averaged $2F_o - F_c$ electron density map (gray mesh, 1.0 σ threshold) for the ordered glycerol molecule and its surrounding amino acids shown in stick presentation and colored as described for panel A for the reference VP3 monomer: C in cyan, N in blue, and O in red for the 5-fold-symmetry-related VP3 monomer; C in yellow and O in red for the glycerol. Distances (in Å) between the glycerol and interacting amino acids are indicated. The images were generated using the PyMol program (http://www.pymol.org).

bonyl of S531 (3.3 Å), the side chain of Q604 (3.8 Å), and the side chain of T711 (4.0 Å [data not shown]) from one VP monomer and with the side chain of D652 (3.1 Å) from the 5-fold-symmetry-related HI loop (Fig. 4B). The backbone atoms of residues 531 to 533 make van der Waals contacts with the hydrophobic side of the glycerol molecule (Fig. 4B). While a function for the AAV5-glycerol interaction is unknown, a protein-stabilizing role for glycerol is well established (74, 75). The localization of this ligand between two surface loops which differ in structure between AAV5 and the other AAVs, VR-VII and HI, with VR-VII being significantly larger than in the other viruses (Fig. 4A), suggests that the glycerol may also be playing a stabilizing role in AAV5. Interestingly, this glycerol binding site is very reminiscent of a recently reported glycerol binding site in the structure of the succinyl-coenzyme A (CoA):3-oxoacid coenzyme A transferase (76). In this structure the glycerol was reported to be occupying a cosubstrate, acetoacetate, binding site in the enzyme, and it participates in similar side-chain and main-chain hydrogen bonding interactions. Therefore, it is possible that the ordered glycerol molecule is located at a substrate-ligand interaction unique to AAV5.

The assignment of Na^+ ions was based on a high sigma threshold (3.5 σ) for their densities, their monovalent polar coordination environment, and their low B factors (23.5, 8.9, and 14.5 $Å^2$) (average B factors are given Table 1) following refinement. To confirm that the atoms were sodium ions, and not Mg^{2+} and Ca^{2+}, they were replaced and refined independently in addition to an evaluation of the environment. These atoms refined as Mg^{2+} with acceptable B factors (34.9, 19.2, and 25.4 $Å^2$) but not Ca^{2+} (75.8, 61.17, and 67.6 $Å^2$); however, the amino acid environment and interactions were more consistent with monovalency. The first Na^+ (Na^+1 in Fig. 4A) is located between residues at the top of the βB strand and the HI loop on the capsid surface and is coordinated by the side chain of residue N243 (3.5 Å), the second Na^+ ion (Na^+2 in Fig. 4A) is located in the capsid interior and interacts with the main-chain carbonyl oxygen of N407 (3.7 Å) in the βG strand, and the third ion (Na^+3 in Fig. 4A) interacts with main-chain carbonyl oxygen of residue T541 (3.9 Å) located in VR-VII. Roles for these Na^+ ions have not been reported. However, the surface ions Na^+1 and Na^+3 are likely playing stabilizing roles for the AAV5 HI loop and VR-VII, respectively, maintaining the unique surface configuration of AAV5 on its shallow canyon floor surrounding the 5-fold channel.

Unique AAV5 surface features are associated with AAV capsid functions. AAV entry is initiated by cell surface receptor recognition, and for seven of the nine representative AAV serotypes, glycans have been reported to serve as primary receptors. AAV1 binds both α2-3 and α2-6 N-linked sialic acid (SIA) (77–79), AAV2 and AAV3B bind to heparan sulfate (HS) (80, 81), AAV4 binds α2-3 O-linked sialic acids, AAV5 binds α2-3 N-linked SIA (82–84), AAV6 binds both HS and SIA (78, 85), and AAV9 binds to galactose (86–88). The glycan receptor (if any) utilized by AAV7 and AAV9 is yet to be determined. Following primary receptor attachment, virus capsids are internalized by receptor-mediated endocytosis via an interaction with coreceptors and trafficked through the endocytic pathway before localizing in the perinuclear region prior to entry into the nucleus for genome replication (reviewed in references 51 and 72). For AAV5, platelet-derived growth factor receptor (PDGFRα) serves as its internalization coreceptor (89). Capsid assembly and genome packaging occur in the nucleus following protein translation in the cytoplasm.

The VRs defined on the AAV capsids are associated with serotype-specific functions during infection, including receptor recognition, tissue transduction efficiency, and antigenic reactivity (reviewed in reference 51). The AAV capsid surface features that are unique to AAV5—shorter 3-fold protrusions, extended VR-VII, and smaller HI loop—contain amino acid residues or are proximate to capsid regions reported to play essential roles in the AAV life cycle. For example, residues within VR-IV, VR-V, and VR-VIII which make up the 3-fold protrusions have been reported to control glycan receptor attachment (VR-V and VR-VIII for AAV2 and VR-V for AAV9) (90–93, 122), transduction (VR-IV, VR-V, and VR-VIII in AAV2, VR-VIII in AAV8, and VR-IV, VR-V, and VR-VIII in AAV9) (94–99) and antigenic phenotypes (VR-IV, VR-V, and VR-VIII in AAV2 and VR-VIII in AAV8 (97, 100, 101). These regions have similar roles in AAV5. In a study aimed at identifying determinants of human airway epithelium (HAE) transduction by AAV5, a chimeric AAV2/AAV5 virus,

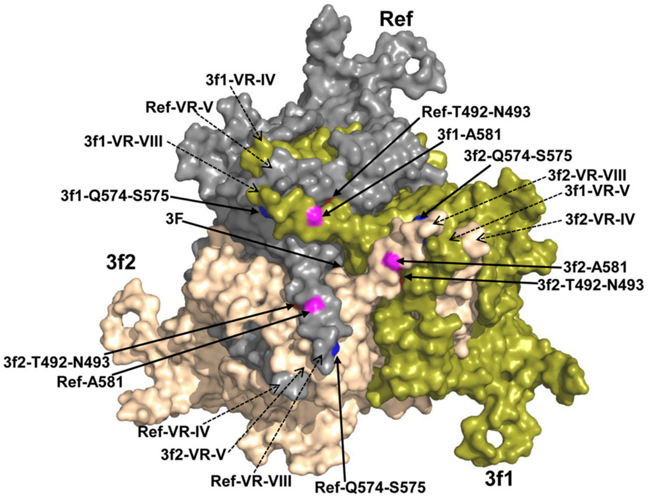

FIG 5 Reported determinants of AAV5 capsid assembly, receptor recognition, and transduction. An exterior capsid surface representation for an AAV5 VP3 trimer in gray (Ref, reference), green (3f1, 3-fold), and salmon (3f2, 3-fold). Surface regions of the VP3 monomers with the amino acid deletions (T492 to N493, red) or duplications (T492, red; Q574 to S575, blue) investigated by Hida et al. (113) are indicated by arrows and labeled. Residue A581, which when mutated to T affects AAV5 sialic acid binding by AAV5 and capsid internalization (102, 103), is shown in pink and labeled. VR-IV, VR-V, and VR-VIII, which interact from 3-fold-symmetry VP3 monomers to assemble the protrusions surrounding this axis (3F), are indicated by the dashed arrows with the open heads. This image was generated using the CHIMERA program (118).

AAV2.5T, containing amino acids 1 to 128 from AAV2 and amino acids 129 to 725 from AAV5 with a single point mutation (A581T, in VR-VIII) showed 100- and 10-fold higher expression levels than AAV2 and AAV5, respectively (102). Residue A581 was reported to play a role in SIA recognition and internalization by AAV5 (102, 103) and forms a part of a new structurally defined SIA binding site (M. A. DiMattia, J. A. Chiorini, and M. Agbandje-McKenna, unpublished data). This residue is located on the capsid surface proximal to the icosahedral 3-fold axis (Fig. 5). Residues within VR-VII are implicated in AAV2 antibody recognition properties (97), and for AAV9, residues in VR-VII were identified as a transduction determinant (95). The unique structure of VR-VII in AAV5 suggests that it may also serve a similar function in this serotype.

The short HI loop (between βH and βI, residues 644 to 658) in AAV5, compared to that in AAV2 and AAV4, is due to a threonine deletion between residues 649 and 650 (AAV5 numbering) (Fig. 3B). Substitution of this shorter HI loop into the AAV2 VP sequence was reported to disrupt AAV2 capsid assembly, while substitution with the AAV4 HI loop, similar in size but with sequence variation, resulted in a decreased titer (104). Replacement of this loop with a glycine peptide in AAV2 resulted in a defect in packaging, and the mutation of a sequence and structurally conserved phenylalanine residue (F661 in AAV2 and F650 in AAV5) decreased packaging by 10-fold. These observations suggest a critical role for this loop region in AAV infection.

There are also reports that mutation of AAV2 residues in the 5-fold channel, structurally adjacent to the HI loop, both in the β-ribbons that extend outward (with VR-II at its apex) and the residues on the interior narrow region of the channel, results in an inability of the capsid to package its genome (105, 106). It has been suggested that this is principally due to altered Rep-VP complexes that form at the 5-fold channel, proposed to be the portal for DNA packaging. Rep proteins bind to the inverted terminal repeats (ITRs) of the AAV genome and also to an unknown binding site on the assembled-capsid surface (107–110). Although AAV5 Rep has been reported to bind a distinct terminal resolution site (TRS) site found only in the AAV5 ITR (3), cross-packing experiments suggest that AAV2 Rep is able to interact with an AAV5 capsid sufficiently to allow packaging of an AAV2 genome into an AAV5 capsid (15). However, mutagenesis studies implicating AAV2 capsid surface residues 511 to 513 (near VR-VI, AAV2 numbering) (111) and 549 (in VR-VII) (112) in packaging suggests that the AAV2 capsid-AAV2 Rep interaction would differ from an interaction with the AAV5 Rep. Significantly, the HI loop and VR-VII structurally abut in 5-fold-symmetry-related VP3 monomers (Fig. 4A). Thus, it is possible that the 5-fold region, as a whole, functions to facilitate genome packaging.

The structure of AAV5 also provides a 3D platform for the interpretation of the phenotype of capsid mutants (within VR regions) that were generated with the intent to produce vectors able to escape antibody recognition and have improved transduction phenotypes. In a mutagenesis strategy aimed at creating AAV5 mutant capsids with insertions and deletions, Hida et al. generated four mutants, two with residue duplications (at residues 492 and 574 to 575) and two with deletions (of residues 176 to 178 and 492 to 493) (113). N-terminal residues 176 to 178 are within the VP1/VP2 common region that is not observed in any of the AAV structures determined to date. The other amino acid positions are located on the protrusions that surround the icosahedral 3-fold axes and are at interfaces between symmetry-related VP3 monomers (Fig. 5). Residue T492 is involved in a polar interaction with residues K494 and Q503 from the same monomer, N493 interacts with the side and main chains of M569 and A570, respectively, and Q574 interacts with the side chain of N482 from a symmetry-related monomer. The side chain for S575 is surface exposed and does not interact with any other residue. The duplicated T492 mutant is unable to assemble capsids, suggesting a possible intolerance of the crowding of the VP interface. The deletion of residues 492 to 493 was tolerated for capsid assembly, but transduction was either undetectable or significantly (~24-fold) reduced. The duplication of residues 574 to 575, located in VR-VIII, was tolerated for capsid assembly and resulted in an increase in transduction compared to the wild-type virus. Significantly, the side chain of residues 492 and 494, at the end of VR-V, are located between the loops containing VR-IV and VR-VIII, and their side chains point into the 3-fold protrusion. The side chain of residue 574 also points inside the 3-fold protrusion to interact with residue 482 located at the more structurally varied end of VR-V, consistent with tolerance of this mutation for capsid assembly. Q574 is structurally equivalent to R585 of AAV2, one of the residues involved in its HS receptor binding, and is located at a region that has been reported to tolerate insertions for the latter virus. These mutants thus identified a critical region of the capsid involved in capsid assembly interactions, tolerance of insertional mutagenesis, and transduction determination, possibly related to receptor attachment.

Comparison of AAV5 to nonprimate AAV-Go.1 highlights potential transduction and antigenic determinants. A theoretical homology model generated for nonprimate AAV-Go.1, re-

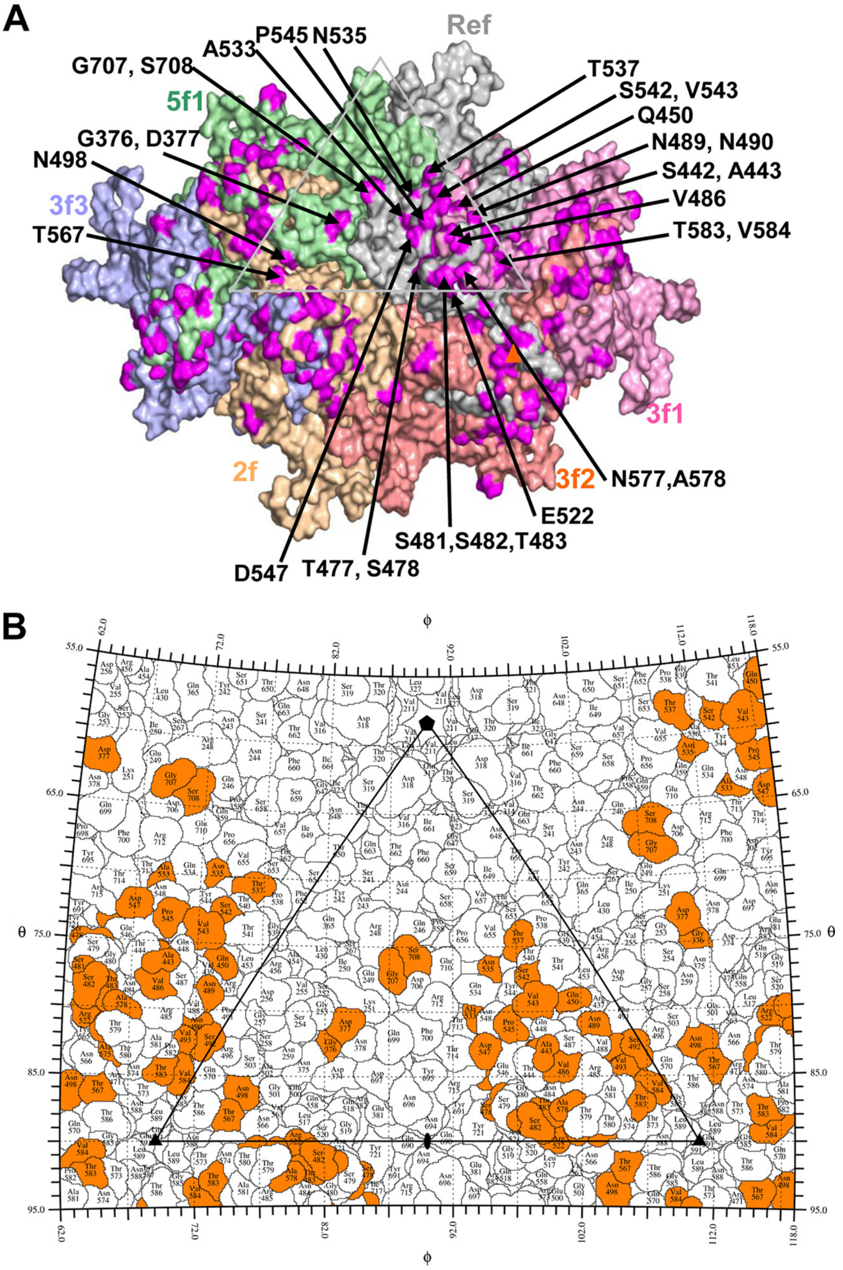

FIG 6 A model of AAV-Go.1 based on the AAV5 VP3 structure. (A) A surface representation of six VP3 monomers, including the reference (Ref) monomer in gray, of the AAV-Go.1 homology model. Residues differing between AAV5 and AAV-Go.1 and occurring on the capsid surface are shown in purple, indicated with arrows, and labeled. These cluster on the 3-fold protrusions and the raised capsid region between the depression at the 2-fold axis and surrounding the 5-fold axis. The light gray triangle depicts the viral asymmetric unit as defined in the legend of Fig. 2. (B). A Roadmap (68) representation of the AAV-Go.1 model showing the capsid surface positions of the residues that differ with respect to AAV5 in the context of a viral asymmetric unit (black triangle). The residues that differ between AAV5 and AAV-Go.1 are shown in orange. Panel A was generated with the PyMol program (http://www.pymol.org), and panel B was generated with the RIVEM program (68).

ported to be more related to AAV5 than other serotypes (13) and than AAV2 and AAV4, identifies regions of structural similarities and differences. A superposition of the Cα atoms for the model with the structures of AAV2 and AAV5 showed conservation of the AAV VP topology, including the eight-stranded β-barrel motif, αA, and loops between the β-strands as described above. While AAV-Go.1 differed from AAV2 at the same VRs as AAV5, this virus, which shares ~94% sequence identity with AAV5, differed only in VR-V compared to AAV5. This difference was due to a 2-amino-acid insertion in AAV-Go.1 (residues 481 and 482) (13) relative to AAV5. Variable region V is located between VR-IV and VR-VIII, and together these loop regions assemble the protrusions surrounding the icosahedral 3-fold axis (Fig. 5). AAV-Go.1 differs in 42 of the 724 AAV5 amino acids, and while the AAV5/AAV-Go.1 residue differences are distributed throughout the VP sequence, 29 of the 42 are located on the capsid surface. These are clustered on these protrusions and on the raised capsid region between the 2- and 5-fold depressions (Fig. 6). The surface exposure of these residues was also predicted based on a model by Arbetman et al. (13). The surface-localized residues occupy analogous regions to those mapped as antigenic footprints on other AAV capsids, for example, AAV2 and AAV8 (97, 100, 101, 114), and thus likely dictate the antigenic differences reported between the two viruses when their transduction efficiencies were compared in the presence of intravenous immunoglobulin (13).

Internal capsid volumes are comparable between AAV2, AAV4, and AAV5 and do not support an increased packaging capacity for AAV5 compared to other AAVs. A report that AAV5 is able to package a genome of ~8.9 kb (53) was later disputed with reports of a packaging capacity of ~5.2 kb (54–56). The latter reports suggested that expression of the large transgenes were likely the result of recombination of smaller packaged genome fragments rather than the packaging of the full-length large genome. The estimated interior capsid volumes for AAV2, AAV4, and AAV5, based on radii calculated from their structures, are $\sim 3.4 \times 10^6$, $\sim 3.1 \times 10^6$, and $\sim 3.1 \times 10^6$ Å^3, respectively, which are very similar. This observation is consistent with AAV5 not having approximately double the genome packaging capacity of the other AAVs. Significantly, *Human parvovirus* B19, a member of the *Erythrovirus* genus of the *Parvoviridae*, packages a genome of ~5.6 kb of ssDNA, which is slighter higher (~20%) than the wild-type AAV packaging capacity. The estimated interior capsid volume for B19 is 3.2×10^6 Å^3, which is in the same range as for the AAVs. A comparable interior capsid volume for the AAVs (and other members of the parvovirus family) is to be expected, given that the βBIDG sheet that assembles their interior capsid surface is conserved and almost exactly superposable for the ordered VP3 common region (Fig. 1B and 3A). The ability of the B19 capsid to accommodate more genome than the AAVs may be due to more available interior capsid space; its VP1u and VP2 N terminus are reported to be located on the exterior of the capsid (71) in contrast to the AAVs, where these VP regions are proposed to be localized inside. However, it is also possible to package ~6 kb into the recombinant AAV vectors (115, 116).

Nucleic acid-protein interactions are mostly electrostatic and involve the negatively charged phosphate groups of the DNA and basic amino acid residues or the heterocyclic DNA bases and acidic amino acid residues. Thus, the exterior and interior capsid surface charge distributions were visualized and compared for AAV5, AAV2, AAV4, and B19 (data not shown). There was no significant difference between the net exterior and interior capsid surface charge distributions for these viruses, suggesting that the size of the packaged genome is likely not dictated by these interactions. Notably, the charge contributions of the VP1u and VP1/VP2 common regions were missing from the AAV and B19 estimations, and their contribution cannot be ruled out. These observations are interesting, and the importance of interior charge residues in increasing DNA packaging capacity, especially for the parvoviruses which package their genome after capsid assembly (117), needs further exploration.

Summary. The structure of AAV5, one of the most diverse AAV serotypes with respect to sequence and antigenic diversity, was determined to further facilitate structure-function correlations for this promising group of gene delivery vectors. Unique features of the AAV5 capsid surface, including a smaller HI and VR-IV loop and larger VR-VII, are contained in VP sequences important for essential functions, including capsid assembly, genome packaging, and transduction and antigenic determinants. In addition, the surface amino acid differences between AAV5 and the closely related AAV-Go.1 point to regions that likely serve as important antigenic and transduction determinants. Finally, volume calculations do not support an increased packaging capacity for this serotype. This structure provides an important new 3D platform for future efforts to engineer the cellular transduction and antigenic properties of the AAV gene delivery system.

ACKNOWLEDGMENTS

We thank the staff at the X29 beamline at NSLS, Brookhaven National Laboratory, SER-CAT 22-ID Beamline, Advanced Photon Source, Argonne National Laboratory, and the F1 beamline at CHESS, Cornell University, for help during data collection. We especially thank Kathy Dedrick at CHESS for assistance in obtaining beam time.

The NSLS is supported by the U.S. Department of Energy, Office of Science, Office of Basic Energy Sciences, under contract number DE-AC02-98CH10886. Use of the Advanced Photon Source was supported by the U.S. Department of Energy, Basic Energy Sciences, Office of Science, under contract number W-31-109-Eng-38. CHESS is supported by the National Science Foundation and the National Institutes of Health/National Institute of General Medical Sciences under NSF award DMR-0936384 and the MacCHESS facility through award GM-103485 from the National Institute of General Medical Sciences, National Institutes of Health. This research was supported by the Intramural Research Program of the NIH and NIDCR to J.A.C. and NIH R01 GM082946 (M.A.-M., R.M., N.M., and S.Z.) and P01 HL51811 (M.A.-M., R.M., and N.M.).

REFERENCES

1. **Flotte TR, Carter BJ.** 1995. Adeno-associated virus vectors for gene therapy. Gene Ther. **2:**357–362.
2. **Mingozzi F, High KA.** 2011. Therapeutic in vivo gene transfer for genetic disease using AAV: progress and challenges. Nat. Rev. Genet. **12:**341–355.
3. **Chiorini JA, Afione S, Kotin RM.** 1999. Adeno-associated virus (AAV) type 5 Rep protein cleaves a unique terminal resolution site compared with other AAV serotypes. J. Virol. **73:**4293–4298.
4. **Chiorini JA, Kim F, Yang L, Kotin RM.** 1999. Cloning and characterization of adeno-associated virus type 5. J. Virol. **73:**1309–1319.
5. **Gao GP, Alvira MR, Wang L, Calcedo R, Johnston J, Wilson JM.** 2002. Novel adeno-associated viruses from rhesus monkeys as vectors for human gene therapy. Proc. Natl. Acad. Sci. U. S. A. **99:**11854–11859.
6. **Muramatsu S, Mizukami H, Young NS, Brown KE.** 1996. Nucleotide sequencing and generation of an infectious clone of adeno-associated virus 3. Virology **221:**208–217.
7. **Rutledge EA, Halbert CL, Russell DW.** 1998. Infectious clones and vectors derived from adeno-associated virus (AAV) serotypes other than AAV type 2. J. Virol. **72:**309–319.
8. **Srivastava A, Lusby EW, Berns KI.** 1983. Nucleotide sequence and organization of the adeno-associated virus 2 genome. J. Virol. **45:**555–564.
9. **Atchison RW, Casto BC, Hammon WM.** 1965. Adenovirus-associated defective virus particles. Science **149:**754–756.
10. **Mori S, Wang L, Takeuchi T, Kanda T.** 2004. Two novel adeno-associated viruses from cynomolgus monkey: pseudotyping characterization of capsid protein. Virology **330:**375–383.
11. **Schmidt M, Voutetakis A, Afione S, Zheng C, Mandikian D, Chiorini JA.** 2008. Adeno-associated virus type 12 (AAV12): a novel AAV serotype with sialic acid- and heparan sulfate proteoglycan-independent transduction activity. J. Virol. **82:**1399–1406.
12. **Schmidt M, Katano H, Bossis I, Chiorini JA.** 2004. Cloning and characterization of a bovine adeno-associated virus. J. Virol. **78:**6509–6516.
13. **Arbetman AE, Lochrie M, Zhou S, Wellman J, Scallan C, Doroudchi MM, Randlev B, Patarroyo-White S, Liu T, Smith P, Lehmkuhl H, Hobbs LA, Pierce GF, Colosi P.** 2005. Novel caprine adeno-associated virus (AAV) capsid (AAV-Go. 1) is closely related to the primate AAV-5 and has unique tropism and neutralization properties. J. Virol. **79:**15238–15245.
14. **Lochrie MA, Tatsuno GP, Arbetman AE, Jones K, Pater C, Smith PH, McDonnell JW, Zhou SZ, Kachi S, Kachi M, Campochiaro PA, Pierce**

GF, Colosi P. 2006. Adeno-associated virus (AAV) capsid genes isolated from rat and mouse liver genomic DNA define two new AAV species distantly related to AAV-5. Virology **353**:68–82.
15. **Gao G, Vandenberghe LH, Alvira MR, Lu Y, Calcedo R, Zhou X, Wilson JM.** 2004. Clades of adeno-associated viruses are widely disseminated in human tissues. J. Virol. **78**:6381–6388.
16. **McLaughlin SK, Collis P, Hermonat PL, Muzyczka N.** 1988. Adeno-associated virus general transduction vectors: analysis of proviral structures. J. Virol. **62**:1963–1973.
17. **Samulski RJ, Srivastava A, Berns KI, Muzyczka N.** 1983. Rescue of adeno-associated virus from recombinant plasmids: gene correction within the terminal repeats of AAV. Cell **33**:135–143.
18. **Samulski RJ, Chang LS, Shenk T.** 1987. A recombinant plasmid from which an infectious adeno-associated virus genome can be excised in vitro and its use to study viral replication. J. Virol. **61**:3096–3101.
19. **Senapathy P, Tratschin JD, Carter BJ.** 1984. Replication of adeno-associated virus DNA. Complementation of naturally occurring *rep*$^-$ mutants by a wild-type genome or an *ori*$^-$ mutant and correction of terminal palindrome deletions. J. Mol. Biol. **179**:1–20.
20. **Kronenberg S, Kleinschmidt JA, Bottcher B.** 2001. Electron cryo-microscopy and image reconstruction of adeno-associated virus type 2 empty capsids. EMBO Rep. **2**:997–1002.
21. **Xie Q, Bu W, Bhatia S, Hare J, Somasundaram T, Azzi A, Chapman MS.** 2002. The atomic structure of adeno-associated virus (AAV-2), a vector for human gene therapy. Proc. Natl. Acad. Sci. U. S. A. **99**:10405–10410.
22. **Govindasamy L, Padron E, McKenna R, Muzyczka N, Kaludov N, Chiorini JA, Agbandje-McKenna M.** 2006. Structurally mapping the diverse phenotype of adeno-associated virus serotype 4. J. Virol. **80**:11556–11570.
23. **Lerch TF, Xie Q, Chapman MS.** 2010. The structure of adeno-associated virus serotype 3B (AAV-3B): insights into receptor binding and immune evasion. Virology **403**:26–36.
24. **Walters RW, Agbandje-McKenna M, Bowman VD, Moninger TO, Olson NH, Seiler M, Chiorini JA, Baker TS, Zabner J.** 2004. Structure of adeno-associated virus serotype 5. J. Virol. **78**:3361–3371.
25. **Padron E, Bowman V, Kaludov N, Govindasamy L, Levy H, Nick P, McKenna R, Muzyczka N, Chiorini JA, Baker TS, Agbandje-McKenna M.** 2005. Structure of adeno-associated virus type 4. J. Virol. **79**:5047–5058.
26. **Ng R, Govindasamy L, Gurda BL, McKenna R, Kozyreva OG, Samulski RJ, Parent KN, Baker TS, Agbandje-McKenna M.** 2010. Structural characterization of the dual glycan binding adeno-associated virus serotype 6. J. Virol. **84**:12945–12957.
27. **DiMattia MA, Nam HJ, Van Vliet K, Mitchell M, Bennett A, Gurda BL, McKenna R, Olson NH, Sinkovits RS, Potter M, Byrne BJ, Aslanidi G, Zolotukhin S, Muzyczka N, Baker TS, Agbandje-McKenna M.** 2012. Structural insight into the unique properties of adeno-associated virus serotype 9. J. Virol. **86**:6947–6958.
28. **Kronenberg S, Bottcher B, von der Lieth CW, Bleker S, Kleinschmidt JA.** 2005. A conformational change in the adeno-associated virus type 2 capsid leads to the exposure of hidden VP1 N termini. J. Virol. **79**:5296–5303.
29. **Nam HJ, Lane MD, Padron E, Gurda B, McKenna R, Kohlbrenner E, Aslanidi G, Byrne B, Muzyczka N, Zolotukhin S, Agbandje-McKenna M.** 2007. Structure of adeno-associated virus serotype 8, a gene therapy vector. J. Virol. **81**:12260–12271.
30. **Flannery JG, Zolotukhin S, Vaquero MI, LaVail MM, Muzyczka N, Hauswirth WW.** 1997. Efficient photoreceptor-targeted gene expression in vivo by recombinant adeno-associated virus. Proc. Natl. Acad. Sci. U. S. A. **94**:6916–6921.
31. **Flotte TR.** 2005. Recent developments in recombinant AAV-mediated gene therapy for lung diseases. Curr. Gene Ther. **5**:361–366.
32. **Herzog RW.** 2004. AAV-mediated gene transfer to skeletal muscle. Methods Mol. Biol. **246**:179–194.
33. **Niemeyer GP, Herzog RW, Mount J, Arruda VR, Tillson DM, Hathcock J, van Ginkel FW, High KA, Lothrop CD, Jr.** 2009. Long-term correction of inhibitor-prone hemophilia B dogs treated with liver-directed AAV2-mediated factor IX gene therapy. Blood **113**:797–806.
34. **Maguire AM, Simonelli F, Pierce EA, Pugh EN, Jr, Mingozzi F, Bennicelli J, Banfi S, Marshall KA, Testa F, Surace EM, Rossi S, Lyubarsky A, Arruda VR, Konkle B, Stone E, Sun J, Jacobs J, Dell'Osso L, Hertle R, Ma JX, Redmond TM, Zhu X, Hauck B, Zelenaia O, Shindler KS, Maguire MG, Wright JF, Volpe NJ, McDonnell JW, Auricchio A, High KA, Bennett J.** 2008. Safety and efficacy of gene transfer for Leber's congenital amaurosis. N. Engl. J. Med. **358**:2240–2248.
35. **Buch PK, Bainbridge JW, Ali RR.** 2008. AAV-mediated gene therapy for retinal disorders: from mouse to man. Gene Ther. **15**:849–857.
36. **Cideciyan AV.** 2010. Leber congenital amaurosis due to RPE65 mutations and its treatment with gene therapy. Prog. Retin. Eye Res. **29**:398–427.
37. **Cideciyan AV, Hauswirth WW, Aleman TS, Kaushal S, Schwartz SB, Boye SL, Windsor EA, Conlon TJ, Sumaroka A, Pang JJ, Roman AJ, Byrne BJ, Jacobson SG.** 2009. Human RPE65 gene therapy for Leber congenital amaurosis: persistence of early visual improvements and safety at 1 year. Hum. Gene Ther. **20**:999–1004.
38. **Dinculescu A, Estreicher J, Zenteno JC, Aleman TS, Schwartz SB, Huang WC, Roman AJ, Sumaroka A, Li Q, Deng WT, Min SH, Chiodo VA, Neeley A, Liu X, Shu X, Matias-Florentino M, Buentello-Volante B, Boye SL, Cideciyan AV, Hauswirth WW, Jacobson SG.** 2012. Gene therapy for retinitis pigmentosa caused by MFRP mutations: human phenotype and preliminary proof of concept. Hum. Gene Ther. **23**:367–376.
39. **Jacobson SG, Acland GM, Aguirre GD, Aleman TS, Schwartz SB, Cideciyan AV, Zeiss CJ, Komaromy AM, Kaushal S, Roman AJ,Windsor EA, Sumaroka A, Pearce-Kelling SE, Conlon TJ, Chiodo VA, Boye SL, Flotte TR, Maguire AM, Bennett J, Hauswirth WW.** 2006. Safety of recombinant adeno-associated virus type 2-RPE65 vector delivered by ocular subretinal injection. Mol. Ther. **13**:1074–1084.
40. **Jacobson SG, Boye SL, Aleman TS, Conlon TJ, Zeiss CJ, Roman AJ, Cideciyan AV, Schwartz SB, Komaromy AM, Doobrajh M, Cheung AY, Sumaroka A, Pearce-Kelling SE, Aguirre GD, Kaushal S, Maguire AM, Flotte TR, Hauswirth WW.** 2006. Safety in nonhuman primates of ocular AAV2-RPE65, a candidate treatment for blindness in Leber congenital amaurosis. Hum. Gene Ther. **17**:845–858.
41. **Mendell JR, Rodino-Klapac L, Sahenk Z, Malik V, Kaspar BK, Walker CM, Clark KR.** 2012. Gene therapy for muscular dystrophy: lessons learned and path forward. Neurosci. Lett. **527**:90–99.
42. **Mendell JR, Rodino-Klapac LR, Rosales XQ, Coley BD, Galloway G, Lewis S, Malik V, Shilling C, Byrne BJ, Conlon T, Campbell KJ, Bremer WG, Taylor LE, Flanigan KM, Gastier-Foster JM, Astbury C, Kota J, Sahenk Z, Walker CM, Clark KR.** 2010. Sustained alpha-sarcoglycan gene expression after gene transfer in limb-girdle muscular dystrophy, type 2D. Ann. Neurol. **68**:629–638.
43. **Virella-Lowell I, Zusman B, Foust K, Loiler S, Conlon T, Song S, Chesnut KA, Ferkol T, Flotte TR.** 2005. Enhancing rAAV vector expression in the lung. J. Gene Med. **7**:842–850.
44. **Zabner J, Seiler M, Walters R, Kotin RM, Fulgeras W, Davidson BL, Chiorini JA.** 2000. Adeno-associated virus type 5 (AAV5) but not AAV2 binds to the apical surfaces of airway epithelia and facilitates gene transfer. J. Virol. **74**:3852–3858.
45. **Burger C, Gorbatyuk OS, Velardo MJ, Peden CS, Williams P, Zolotukhin S, Reier PJ, Mandel RJ, Muzyczka N.** 2004. Recombinant AAV viral vectors pseudotyped with viral capsids from serotypes 1, 2, and 5 display differential efficiency and cell tropism after delivery to different regions of the central nervous system. Mol. Ther. **10**:302–317.
46. **Nathwani AC, Gray JT, McIntosh J, Ng CY, Zhou J, Spence Y, Cochrane M, Gray E, Tuddenham EG, Davidoff AM.** 2007. Safe and efficient transduction of the liver after peripheral vein infusion of self-complementary AAV vector results in stable therapeutic expression of human FIX in nonhuman primates. Blood **109**:1414–1421.
47. **Duan D, Yan Z, Yue Y, Ding W, Engelhardt JF.** 2001. Enhancement of muscle gene delivery with pseudotyped adeno-associated virus type 5 correlates with myoblast differentiation. J. Virol. **75**:7662–7671.
48. **Lipshutz GS, Titre D, Brindle M, Bisconte AR, Contag CH, Gaensler KM.** 2003. Comparison of gene expression after intraperitoneal delivery of AAV2 or AAV5 in utero. Mol. Ther. **8**:90–98.
49. **Auricchio A, O'Connor E, Weiner D, Gao GP, Hildinger M, Wang L, Calcedo R, Wilson JM.** 2002. Noninvasive gene transfer to the lung for systemic delivery of therapeutic proteins. J. Clin. Invest. **110**:499–504.
50. **Lin DS, Hsiao CD, Liau I, Lin SP, Chiang MF, Chuang CK, Wang TJ, Wu TY, Jian YR, Huang SF, Liu HL.** 2011. CNS-targeted AAV5 gene transfer results in global dispersal of vector and prevention of morphological and function deterioration in CNS of globoid cell leukodystrophy mouse model. Mol. Genet. Metab. **103**:367–377.

51. **Agbandje-McKenna M, Kleinschmidt J.** 2011. AAV capsid structure and cell interactions. Methods Mol. Biol. **807:**47–92.
52. **Xie Q, Lerch TF, Meyer NL, Chapman MS.** 2011. Structure-function analysis of receptor-binding in adeno-associated virus serotype 6 (AAV-6). Virology **420:**10–19.
53. **Allocca M, Doria M, Petrillo M, Colella P, Garcia-Hoyos M, Gibbs D, Kim SR, Maguire A, Rex TS, Di Vicino U, Cutillo L, Sparrow JR, Williams DS, Bennett J, Auricchio A.** 2008. Serotype-dependent packaging of large genes in adeno-associated viral vectors results in effective gene delivery in mice. J. Clin. Invest. **118:**1955–1964.
54. **Wu Z, Yang H, Colosi P.** 2010. Effect of genome size on AAV vector packaging. Mol. Ther. **18:**80–86.
55. **Dong B, Nakai H, Xiao W.** 2010. Characterization of genome integrity for oversized recombinant AAV vector. Mol. Ther. **18:**87–92.
56. **Lai Y, Yue Y, Duan D.** 2010. Evidence for the failure of adeno-associated virus serotype 5 to package a viral genome ≥8.2 kb. Mol. Ther. **18:**75–79.
57. **DiMattia M, Govindasamy L, Levy HC, Gurda-Whitaker B, Kalina A, Kohlbrenner E, Chiorini JA, McKenna R, Muzyczka N, Zolotukhin S, Agbandje-McKenna M.** 2005. Production, purification, crystallization and preliminary X-ray structural studies of adeno-associated virus serotype 5. Acta Crystallogr. Sect. F Struct. Biol. Cryst. Commun. **61:**917–921.
58. **Otwinowski Z, Minor W.** 1997. Processing of X-ray diffraction data collected in oscillation mode. Methods Enzymol. **276:**307–326.
59. **Brünger AT, Adams PD, Clore GM, DeLano WL, Gros P, Grosse-Kunstleve RW, Jiang JS, Kuszewski J, Nilges M, Pannu NS, Read RJ, Rice LM, Simonson T, Warren GL.** 1998. Crystallography & NMR system: a new software suite for macromolecular structure determination. Acta Crystallogr. D Biol. Crystallogr. **54:**905–921.
60. **Brünger AT.** 1993. Assessment of phase accuracy by cross validation: the free R value. Methods and applications. Acta Crystallogr. D Biol. Crystallogr. **49:**24–36.
61. **Jones TA, Zou JY, Cowan SW, Kjeldgaard M.** 1991. Improved methods for building protein models in electron density maps and the location of errors in these models. Acta Crystallogr. A **47:**110–119.
62. **Emsley P, Cowtan K.** 2004. Coot: model-building tools for molecular graphics. Acta Crystallogr. D Biol. Crystallogr. **60:**2126–2132.
63. **Laskowski RA, Rullmannn JA, MacArthur MW, Kaptein R, Thornton JM.** 1996. AQUA and PROCHECK-NMR: programs for checking the quality of protein structures solved by NMR. J. Biomol. NMR **8:**477–486.
64. **Adams PD, Afonine PV, Bunkóczi G, Chen VB, Davis IW, Echols N, Headd JJ, Hung LW, Kapral GJ, Grosse-Kunstleve RW, McCoy AJ, Moriarty NW, Oeffner R, Read RJ, Richardson DC, Richardson JS, Terwilliger TC, Zwart PH.** 2010. *PHENIX*: a comprehensive Python-based system for macromolecular structure solution. Acta Crystallogr. D Biol. Crystallogr. **66:**213–221.
65. **Kleywegt GJ, Zou JY, Kjeldgaard M, Jones TA.** 2001. Around O, p 353–356. *In* Rossmann MG, Arnold E (ed), International tables for crystallography, vol F. Kluwer Academic Publishers, Dordrecht, The Netherlands.
66. **Chen VB, Arendall WB, III, Headd JJ, Keedy DA, Immormino RM, Kapral GJ, Murray LW, Richardson JS, Richardson DC.** 2010. MolProbity: all-atom structure validation for macromolecular crystallography. Acta Crystallogr. D Biol. Crystallogr. **66:**12–21.
67. **Krissinel E, Henrick K.** 2004. Secondary-structure matching (SSM), a new tool for fast protein structure alignment in three dimensions. Acta Crystallogr. D Biol. Crystallogr. **60:**2256–2268.
68. **Xiao C, Rossmann MG.** 2007. Interpretation of electron density with stereographic roadmap projections. J. Struct. Biol. **158:**182–187.
69. **Kiefer F, Arnold K, Kunzli M, Bordoli L, Schwede T.** 2009. The SWISS-MODEL repository and associated resources. Nucleic Acids Res. **37:**D387–392.
70. **Larkin MA, Blackshields G, Brown NP, Chenna R, McGettigan PA, McWilliam H, Valentin F, Wallace IM, Wilm A, Lopez R, Thompson JD, Gibson TJ, Higgins DG.** 2007. Clustal W and Clustal X version 2.0. Bioinformatics **23:**2947–2948.
71. **Kaufmann B, Chipman PR, Kostyuchenko VA, Modrow S, Rossmann MG.** 2008. Visualization of the externalized VP2 N termini of infectious human parvovirus B19. J. Virol. **82:**7306–7312.
72. **Halder S, Ng R, Agbandje-McKenna M.** 2012. Parvoviruses: structure and infection. Future Virol. **7:**253–278.
73. **Chapman MS, Agbandje-McKenna M.** 2006. Atomic structure of viral particles, p 107–123. *In* Kerr JR, Cotmore SF, Bloom ME, Linden RM, Parrish CR (ed), Parvoviruses. Hodder Arnold, London, United Kingdom.
74. **Gekko K, Timasheff SN.** 1981. Mechanism of protein stabilization by glycerol: preferential hydration in glycerol-water mixtures. Biochemistry **20:**4667–4676.
75. **Gekko K, Timasheff SN.** 1981. Thermodynamic and kinetic examination of protein stabilization by glycerol. Biochemistry **20:**4677–4686.
76. **Coker SF, Lloyd AJ, Mitchell E, Lewis GR, Coker AR, Shoolingin-Jordan PM.** 2010. The high-resolution structure of pig heart succinyl-CoA:3-oxoacid coenzyme A transferase. Acta Crystallogr. D Biol. Crystallogr. **66:**797–805.
77. **Chen S, Kapturczak M, Loiler SA, Zolotukhin S, Glushakova OY, Madsen KM, Samulski RJ, Hauswirth WW, Campbell-Thompson M, Berns KI, Flotte TR, Atkinson MA, Tisher CC, Agarwal A.** 2005. Efficient transduction of vascular endothelial cells with recombinant adeno-associated virus serotype 1 and 5 vectors. Hum. Gene Ther. **16:**235–247.
78. **Wu Z, Miller E, Agbandje-McKenna M, Samulski RJ.** 2006. α2,3 and α2,6 N-linked sialic acids facilitate efficient binding and transduction by adeno-associated virus types 1 and 6. J. Virol. **80:**9093–9103.
79. **Li W, Zhang L, Wu Z, Pickles RJ, Samulski RJ.** 2011. AAV-6 mediated efficient transduction of mouse lower airways. Virology **417:**327–333.
80. **Summerford C, Samulski RJ.** 1998. Membrane-associated heparan sulfate proteoglycan is a receptor for adeno-associated virus type 2 virions. J. Virol. **72:**1438–1445.
81. **Messina EL, Nienaber J, Daneshmand M, Villamizar N, Samulski J, Milano C, Bowles DE.** 2012. Adeno-associated viral vectors based on serotype 3b use components of the fibroblast growth factor receptor signaling complex for efficient transduction. Hum. Gene Ther. **23:**1031–1042.
82. **Kaludov N, Brown KE, Walters RW, Zabner J, Chiorini JA.** 2001. Adeno-associated virus serotype 4 (AAV4) and AAV5 both require sialic acid binding for hemagglutination and efficient transduction but differ in sialic acid linkage specificity. J. Virol. **75:**6884–6893.
83. **Walters RW, Pilewski JM, Chiorini JA, Zabner J.** 2002. Secreted and transmembrane mucins inhibit gene transfer with AAV4 more efficiently than AAV5. J. Biol. Chem. **277:**23709–23713.
84. **Walters RW, Yi SM, Keshavjee S, Brown KE, Welsh MJ, Chiorini JA, Zabner J.** 2001. Binding of adeno-associated virus type 5 to 2,3-linked sialic acid is required for gene transfer. J. Biol. Chem. **276:**20610–20616.
85. **Wu Z, Asokan A, Grieger JC, Govindasamy L, Agbandje-McKenna M, Samulski RJ.** 2006. Single amino acid changes can influence titer, heparin binding, and tissue tropism in different adeno-associated virus serotypes. J. Virol. **80:**11393–11397.
86. **Bell CL, Vandenberghe LH, Bell P, Limberis MP, Gao GP, Van Vliet K, Agbandje-McKenna M, Wilson JM.** 2011. The AAV9 receptor and its modification to improve in vivo lung gene transfer in mice. J. Clin. Invest. **121:**2427–2435.
87. **Shen S, Bryant KD, Brown SM, Randell SH, Asokan A.** 2011. Terminal N-linked galactose is the primary receptor for adeno-associated virus 9. J. Biol. Chem. **286:**13532–13540.
88. **Shen S, Bryant KD, Sun J, Brown SM, Troupes A, Pulicherla N, Asokan A.** 2012. Glycan binding avidity determines the systemic fate of adeno-associated virus type 9. J. Virol. **86:**10408–10417.
89. **Di Pasquale G, Davidson BL, Stein CS, Martins I, Scudiero D, Monks A, Chiorini JA.** 2003. Identification of PDGFR as a receptor for AAV-5 transduction. Nat. Med. **9:**1306–1312.
90. **O'Donnell J, Taylor KA, Chapman MS.** 2009. Adeno-associated virus-2 and its primary cellular receptor– cryo-EM structure of a heparin complex. Virology **385:**434–443.
91. **Opie SR, Warrington KH, Jr, Agbandje-McKenna M, Zolotukhin S, Muzyczka N.** 2003. Identification of amino acid residues in the capsid proteins of adeno-associated virus type 2 that contribute to heparan sulfate proteoglycan binding. J. Virol. **77:**6995–7006.
92. **Kern A, Schmidt K, Leder C, Muller OJ, Wobus CE, Bettinger K, Von der Lieth CW, King JA, Kleinschmidt JA.** 2003. Identification of a heparin-binding motif on adeno-associated virus type 2 capsids. J. Virol. **77:**11072–11081.
93. **Levy HC, Bowman VD, Govindasamy L, McKenna R, Nash K, Warrington K, Chen W, Muzyczka N, Yan X, Baker TS, Agbandje-McKenna M.** 2009. Heparin binding induces conformational changes in adeno-associated virus serotype 2. J. Struct. Biol. **165:**146–156.
94. **Raupp C, Naumer M, Muller OJ, Gurda BL, Agbandje-McKenna M,**

Kleinschmidt JA. 2012. The threefold protrusions of adeno-associated virus type 8 are involved in cell surface targeting as well as postattachment processing. J. Virol. **86:**9396–9408.
95. **Kotchey NM, Adachi K, Zahid M, Inagaki K, Charan R, Parker RS, Nakai H.** 2011. A potential role of distinctively delayed blood clearance of recombinant adeno-associated virus serotype 9 in robust cardiac transduction. Mol. Ther. **19:**1079–1089.
96. **Pulicherla N, Shen S, Yadav S, Debbink K, Govindasamy L, Agbandje-McKenna M, Asokan A.** 2011. Engineering liver-detargeted AAV9 vectors for cardiac and musculoskeletal gene transfer. Mol. Ther. **19:**1070–1078.
97. **Lochrie MA, Tatsuno GP, Christie B, McDonnell JW, Zhou S, Surosky R, Pierce GF, Colosi P.** 2006. Mutations on the external surfaces of adeno-associated virus type 2 capsids that affect transduction and neutralization. J. Virol. **80:**821–834.
98. **Wu P, Xiao W, Conlon T, Hughes J, Agbandje-McKenna M, Ferkol T, Flotte T, Muzyczka N.** 2000. Mutational analysis of the adeno-associated virus type 2 (AAV2) capsid gene and construction of AAV2 vectors with altered tropism. J. Virol. **74:**8635–8647.
99. **Li W, Asokan A, Wu Z, Van Dyke T, DiPrimio N, Johnson JS, Govindaswamy L, Agbandje-McKenna M, Leichtle S, Redmond DE, Jr, McCown TJ, Petermann KB, Sharpless NE, Samulski RJ.** 2008. Engineering and selection of shuffled AAV genomes: a new strategy for producing targeted biological nanoparticles. Mol. Ther. **16:**1252–1260.
100. **Gurda BL, Raupp C, Popa-Wagner R, Naumer M, Olson NH, Ng R, McKenna R, Baker TS, Kleinschmidt JA, Agbandje-McKenna M.** 2012. Mapping a neutralizing epitope onto the capsid of adeno-associated virus serotype 8. J. Virol. **86:**7739–7751.
101. **Wobus CE, Hugle-Dorr B, Girod A, Petersen G, Hallek M, Kleinschmidt JA.** 2000. Monoclonal antibodies against the adeno-associated virus type 2 (AAV-2) capsid: epitope mapping and identification of capsid domains involved in AAV-2-cell interaction and neutralization of AAV-2 infection. J. Virol. **74:**9281–9293.
102. **Excoffon KJ, Koerber JT, Dickey DD, Murtha M, Keshavjee S, Kaspar BK, Zabner J, Schaffer DV.** 2009. Directed evolution of adeno-associated virus to an infectious respiratory virus. Proc. Natl. Acad. Sci. U. S. A. **106:**3865–3870.
103. **Dickey DD, Excoffon KJ, Koerber JT, Bergen J, Steines B, Klesney-Tait J, Schaffer DV, Zabner J.** 2011. Enhanced sialic acid-dependent endocytosis explains the increased efficiency of infection of airway epithelia by a novel adeno-associated virus. J. Virol. **85:**9023–9030.
104. **DiPrimio N, Asokan A, Govindasamy L, Agbandje-McKenna M, Samulski RJ.** 2008. Surface loop dynamics in adeno-associated virus capsid assembly. J. Virol. **82:**5178–5189.
105. **Bleker S, Pawlita M, Kleinschmidt JA.** 2006. Impact of capsid conformation and Rep.-capsid interactions on adeno-associated virus type 2 genome packaging. J. Virol. **80:**810–820.
106. **Bleker S, Sonntag F, Kleinschmidt JA.** 2005. Mutational analysis of narrow pores at the fivefold symmetry axes of adeno-associated virus type 2 capsids reveals a dual role in genome packaging and activation of phospholipase A2 activity. J. Virol. **79:**2528–2540.
107. **Dubielzig R, King JA, Weger S, Kern A, Kleinschmidt JA.** 1999. Adeno-associated virus type 2 protein interactions: formation of pre-encapsidation complexes. J. Virol. **73:**8989–8998.
108. **King JA, Dubielzig R, Grimm D, Kleinschmidt JA.** 2001. DNA helicase-mediated packaging of adeno-associated virus type 2 genomes into preformed capsids. EMBO J. **20:**3282–3291.
109. **Prasad KM, Trempe JP.** 1995. The adeno-associated virus Rep78 protein is covalently linked to viral DNA in a preformed virion. Virology **214:**360–370.
110. **Prasad KM, Zhou C, Trempe JP.** 1997. Characterization of the Rep78/adeno-associated virus complex. Virology **229:**183–192.
111. **Asokan A, Hamra JB, Govindasamy L, Agbandje-McKenna M, Samulski RJ.** 2006. Adeno-associated virus type 2 contains an integrin α5β1 binding domain essential for viral cell entry. J. Virol. **80:**8961–8969.
112. **Shi W, Arnold GS, Bartlett JS.** 2001. Insertional mutagenesis of the adeno-associated virus type 2 (AAV2) capsid gene and generation of AAV2 vectors targeted to alternative cell-surface receptors. Hum. Gene Ther. **12:**1697–1711.
113. **Hida K, Won SY, Di Pasquale G, Hanes J, Chiorini JA, Ostermeier M.** 2010. Sites in the AAV5 capsid tolerant to deletions and tandem duplications. Arch. Biochem. Biophys. **496:**1–8.
114. **McCraw DM, O'Donnell JK, Taylor KA, Stagg SM, Chapman MS.** 2012. Structure of adeno-associated virus-2 in complex with neutralizing monoclonal antibody A20. Virology **431:**40–49.
115. **Grieger JC, Samulski RJ.** 2005. Packaging capacity of adeno-associated virus serotypes: impact of larger genomes on infectivity and postentry steps. J. Virol. **79:**9933–9944.
116. **Warrington KH, Jr, Gorbatyuk OS, Harrison JK, Opie SR, Zolotukhin S, Muzyczka N.** 2004. Adeno-associated virus type 2 VP2 capsid protein is nonessential and can tolerate large peptide insertions at its N terminus. J. Virol. **78:**6595–6609.
117. **Myers MW, Carter BJ.** 1980. Assembly of adeno-associated virus. Virology **102:**71–82.
118. **Pettersen EF, Goddard TD, Huang CC, Couch GS, Greenblatt DM, Meng EC, Ferrin TE.** 2004. UCSF Chimera—a visualization system for exploratory research and analysis. J. Comput. Chem. **25:**1605–1612.
119. **Esnouf R.** 1999. Further additions to Molscript version 1.4, including reading and contouring of electron-density maps. Acta Crystallogr. D Biol. Crystallogr. **55:**938–940.
120. **Merritt EA, Murphy MEP.** 1994. Raster3D version 2.0: a program for photorealistic molecular graphics. Acta Crystallogr. D Biol. Crystallogr. **50:**869–873.
121. **Merritt EA, Bacon DJ.** 1997. Raster3D-photorealistic molecular graphics. Methods Enzymol. **277:**505–524.
122. **Bell CL, Gurda BL, Van Vliet K, Agbandje-McKenna M, Wilson JM.** 2012. Identification of the galactose binding domain of the adeno-associated virus serotype 9 capsid. J Virol. **86:**7326–7333.